

Article

Atomization of Borosilicate Glass Melts for the Fabrication of Hollow Glass Microspheres

Tobias Helling ^{1,*}, Florian Reischl ¹, Andreas Rosin ² , Thorsten Gerdes ^{1,2,*}  and Walter Krenkel ²¹ Technology Application Center Spiegelau, Deggendorf Institute of Technology, D-94518 Spiegelau, Germany² Keylab Glass Technology, University of Bayreuth, D-95447 Bayreuth, Germany

* Correspondence: tobias.helling@th-deg.de (T.H.); thorsten.gerdes@th-deg.de (T.G.)

Abstract: Direct atomization of a free-flowing glass melt was carried out using a high-speed flame with the aim of producing tiny, self-expanding glass melt droplets to form hollow glass microspheres. Atomization experiments were carried out using a specially adapted free-fall atomizer in combination with a high-power gas burner to achieve sufficient temperatures to atomize the melt droplets and to directly expand them into hollow glass spheres. In addition, numerical simulations were carried out to investigate non-measurable parameters such as hot gas velocities and temperatures in the flame region by the finite volume-based software Star CCM+[®] (v. 2022.1.1), using the Reynolds-Averaged Navier–Stokes (RANS) turbulence and the segregated flow model. To calculate the combustion process, the laminar flamelet method was used. The experiments and simulations indicated that a maximum gas velocity of about 170 m/s was achieved at the point of atomization in the flame. The particle size distribution of the atomized glass droplets, either solid or hollow, ranged from 2 μm to 4 mm. Mean particle sizes in the range of 370 μm to 650 μm were highly dependent on process parameters such as gas velocity. They were in good agreement with theoretically calculated median diameters. The formation of hollow glass microspheres with the proposed concept could be demonstrated. However, only a small fraction of hollow glass spheres was found to be formed. These hollow spheres had diameters up to 50 μm and, as expected, a thin wall thickness.

Keywords: hollow glass microspheres; glass melt atomization; low melting glass; free-fall atomizer; CFD simulation



Citation: Helling, T.; Reischl, F.; Rosin, A.; Gerdes, T.; Krenkel, W. Atomization of Borosilicate Glass Melts for the Fabrication of Hollow Glass Microspheres. *Processes* **2023**, *11*, 2559. <https://doi.org/10.3390/pr11092559>

Academic Editor: Ioannis Spanopoulos

Received: 1 August 2023

Revised: 22 August 2023

Accepted: 24 August 2023

Published: 26 August 2023



Copyright: © 2023 by the authors. Licensee MDPI, Basel, Switzerland. This article is an open access article distributed under the terms and conditions of the Creative Commons Attribution (CC BY) license (<https://creativecommons.org/licenses/by/4.0/>).

1. Introduction

Hollow glass microspheres or glass bubbles are lightweight powders consisting of thin-walled glass spheres. Glass bubbles typically have diameters in the range of 10 μm to 300 μm with wall thicknesses from 2 μm down to the sub-micron range. Silicate or borosilicate glasses are predominantly used for the production of hollow glass microspheres [1–3]. Due to their low thickness-to-diameter ratio, they have unique thermophysical properties [3]. They exhibit compressive strength up to 186 MPa, while their density reaches 0.6 g/cm³ [4]. Due to low thermal conductivity of 0.05 to 0.2 Wm^{−1}K^{−1}, they have good thermal insulation properties [4]. Glass bubbles are currently used for various applications, mainly as fillers in composite materials in construction and automotive industries, mainly for reasons of weight reduction and thermal insulation [4]. They can also enhance mechanical stability of injection-molded products [2].

Over the last few decades, several manufacturing processes for hollow glass microspheres have been developed, mainly based on two basic processes [3,5,6]. According to state of the art manufacturing, the first process step involves the melting of raw glass in which any gas-forming agents, such as sulphates, are trapped in the melt. Normally, these agents are deliberately used in the glass industry for fining, i.e., the removal of any entrapped gas by creating buoyant sulphur dioxide gas bubbles, which rise rapidly in the glass melt and cause smaller gas bubbles to coalesce [7]. In contrast, the production of

hollow glass beads avoids fining as these agents are needed in the subsequent blowing step. Therefore, the non-finished glass melt is rapidly quenched, dried and finally ground into fine glass powder. In the next stage of the process, this fine glass powder is re-melted in a stream of carrier gas to release the trapped fining gases, which expand the softened glass particles into hollow glass beads. After expansion, the bubbles cool and solidify and are then separated from the gas stream [5,6].

Other methods have been used to form hollow glass spheres from molten glass without the need to produce glass powder by grinding as an intermediate product. For example, molten glass has been separated into individual droplets using a high-speed impact wheel [8], or atomized using hot gas or burner nozzles [9]. However, in each of these processes, the formation of glass droplets has always been separated from the formation of hollow glass spheres [8,9]. To date, no attempts have been made to combine atomization and hollow sphere formation in one step. The novelty of this study is the direct production of hollow glass microspheres by atomization of the melt. A special ring burner system has been designed to expand the atomized melt droplets directly into glass bubbles. The main challenge is to obtain sufficiently small particles that can expand within the extremely short residence time in the hot atomization zone.

1.1. Atomizing of Fluids and Melts

In general, atomization of a free-flowing fluid jet can be divided into primary and secondary break-up. In primary break-up, a flowing fluid jet is disaggregated into individual ligaments and droplets. This occurs during the formation of instabilities caused by perturbations of the fluid jet by its surrounding medium [10,11]. During secondary break-up, the formed ligaments and drops disintegrate further into smaller droplets [10]. According to Lohner [12], the secondary break-up plays a minor role in most cases of atomization of molten metals or minerals.

One major driving force of atomization is the friction between the gaseous and liquid phases, caused by their different velocities. The density of the melt supports disintegration by creating turbulent forces within the melt. While the viscosity of the melt tends to resist any change in shape, the viscosity of the atomizing medium transfers the required shear forces towards the phase boundary to achieve disintegration [13]. Therefore, atomization can be intensified by means such as overpressure or additional gas flows to achieve two-phase atomization [12,14]. In the approach of this article, two-phase atomization is used.

Commonly, the dimensionless Weber We number is used to describe fluid mechanical phenomena of two-phase flows for various applications [15,16]. It is also used to characterize atomization processes. It is defined in general form as follows [17]:

$$We = \frac{\rho \cdot d \cdot u^2}{\sigma} \quad (1)$$

The Weber number describes the ratio of the destabilizing force of the fluid's inertia, represented by the density ρ , the hydraulic diameter d , the velocity u of gas or fluid, and the stabilizing force, represented by surface tension σ . As the Weber number increases, the influence of the kinetic forces increases, and the fluid is likely to destabilize [18–20].

Specific variants of the Weber number are used in the literature to describe atomization, as shown in Equations (2)–(5). The subscripts l and g refer to either the liquid or gaseous phase. The relative velocity Δu is defined by the velocity difference between the liquid and gaseous phases with $\Delta u = u_g - u_l$. For single-phase disintegration of a free stream or secondary atomization of droplets, the absolute or relative liquid Weber numbers, We_l as in Equation (2) or $We_{l,rel}$ as in Equation (3) are most commonly used [11,14,21]. In two-phase atomization, the velocity of the liquid plays a minor role, while the kinetic energy of the surrounding gas phase dominates, as expressed in Equations (4) and (5). In gas-driven atomization, the absolute or relative gaseous Weber numbers, We_g or $We_{g,rel}$, are commonly

used to characterize two-phase processes [11,14,20,22–24]. The different variations of the Weber number can be summarized as follows:

$$We_l = \frac{\rho_l \cdot d_l \cdot u_l^2}{\sigma_l} \quad (2)$$

$$We_{l,rel} = \frac{\rho_l \cdot d_l \cdot \Delta u^2}{\sigma_l} \quad (3)$$

$$We_g = \frac{\rho_g \cdot d_l \cdot u_g^2}{\sigma_l} \quad (4)$$

$$We_{g,rel} = \frac{\rho_g \cdot d_l \cdot \Delta u^2}{\sigma_l} \quad (5)$$

For external two-phase atomization, primary breakup is categorized by different flow regimes which can be characterized by the relative Weber number, $We_{g,rel}$, as described by Equation (5). This classification is used in many studies to describe the corresponding breakup mechanisms. According to Dumouchel [11], the regimes are generally classified as Rayleigh breakup ($We_{g,rel} < 25$), membrane-type breakup ($25 < We_{g,rel} < 70$) and fiber-type breakup ($100 < We_{g,rel} < 500$). However, this classification assumes that the viscosity of the liquid is negligible and is, therefore, not strictly valid for viscous liquids or melts. Corresponding classifications for viscous fluids are not available for the atomizer systems considered here [25]. Nevertheless, the Weber number itself can be used as a comparative value for the evaluation of disintegration processes.

Several empirical equations have been developed to calculate the size of particles formed by two-phase atomization as a function of the forming parameters [12,13,20,26–29]. Typically, such equations are based on dimensionless parameters such as Reynolds or Weber number, and/or material-related parameters such as viscosity, density, and surface tension of the melt as well as the atomizing medium. Without in-depth analysis of the forces, they allow the droplet size spectrum to be determined from their median value. In most cases these correlations have been developed for atomization of aqueous or organic liquids by air. The transfer of these correlations to atomization of melts is critical, as little is known about their limits of validity. However, adapted correlations have also been developed for the estimation of particle sizes for melts. The empiric correlation

$$\frac{d_{50,3}}{d_l} = C \left[\frac{\nu_l}{\nu_g} \frac{1}{We_{l,rel}} \left(1 + \frac{1}{GMR} \right) \right]^{0.5} = C \left[\frac{\nu_l}{\nu_g} \frac{\sigma_l}{\rho_l d_l \Delta u^2} \left(1 + \frac{1}{GMR} \right) \right]^{0.5} \quad (6)$$

for calculation of the median particle diameter was developed by Lubanska [26] for the atomization of metal melts and also used by Lohner [12] for mineral and glass melts. It was derived from a similar atomizer system to that used in the present work [12,26–29]. Herein, ν_l and ν_g represent the kinematic viscosities of the melt (l) and atomizing gas (g), and $We_{l,rel}$ represents the relative liquid Weber number according to Equation (3). C is a technical constant which takes into account both the type of atomizer and its geometry. The gas mass ratio (GMR), is defined as

$$GMR = \frac{\dot{M}_g}{\dot{M}_l} \quad (7)$$

with \dot{M}_g and \dot{M}_l being the mass flow rates of the atomizing gas (g) and the melt (l) [12]. With increasing GMR , atomization is intensified, and the median diameter of melt droplets decreases. In summary, the parameters in Equations (6) and (7) can be divided into either process-related (Δu , d_l , \dot{M}_g and \dot{M}_l), or material-related parameters (ν_l , ν_g , ρ_l and σ_l) [12,28,30].

There are only a few types of atomizers described in the literature for atomizing glass melts. The most common one is the so-called free-fall atomizer (see Figure 1). This type of atomizer consists of two ring nozzles, also called primary nozzle and secondary nozzle. The glass melt flows freely through both nozzles by gravity without touching either the primary or the secondary nozzle. This reduces the risk of clogging [12]. The main contribution to atomization is performed by the secondary nozzle. The primary nozzle largely suppresses the gas recirculation induced by the secondary nozzle [31].

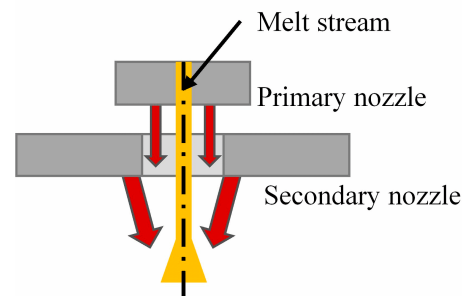
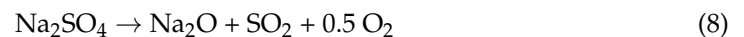


Figure 1. Schematic sketch of free fall atomizer with two nozzle system.

In the present setup, an adapted combustion-driven free-fall atomizer with a gas mixture of methane, oxygen and compressed air is used. Thus, the gas properties depend on both the fuel gas composition and the combustion conditions. In order to analyze the process, principles and models of non-fuel driven atomizers are compared with the developed fuel-driven (hot gas) atomizer and their validity is checked.

1.2. Glass Bubble Formation

As explained above, micro hollow glass spheres are formed using agents that usually decompose at high temperatures. A common refining agent is sodium sulphate (Na_2SO_4), which melts at 1157 K [1,2]. In viscous glass melts the Na_2SO_4 decomposes according to



above 1673 K [1,2]. The decomposition process is highly dependent on the oxidation state of the glass melt, as at these temperatures the reaction only takes place under oxidizing or slightly reducing conditions [1]. For manufacturing of hollow microspheres, it is beneficial to use a low-melting, oxidizing glass in order to achieve decomposition of Na_2SO_4 after atomization within the range of flame temperatures [1,2]. Lohner et al. reported the successful atomization of a glass melt using hot gas and steam at temperatures up to 1073 K [28]. However, the disadvantage is that such a gas temperature would be too low to initiate bubble formation. Therefore, our aim was to achieve high flame temperatures for in-situ formation of hollow glass microspheres following direct melt atomization.

2. Materials and Methods

The feasibility of the process was tested using an alkali-rich borosilicate glass (model glass), consisting of SiO_2 (45 wt%), B_2O_3 (25 wt%), Na_2O (10 wt%), K_2O (10 wt%), CaO (5 wt%), Al_2O_3 (2.5 wt%) and ZnO (2.5 wt%). The amount of the refining agent was 1 wt% SO_3 , based on the mass of the glass. The purpose of using this model glass was to perform melt atomization with a preferably low viscous fluid (ν_1) and low surface tension (σ_1) in order to reduce the droplet size according to Equation (6). The dynamic viscosity of the glass was measured by rotational viscometry (MCR 302, Anton Paar GmbH, Graz, Austria). The surface tension was calculated using the SciGlass Professional[®] (v. 7.11, AKos GmbH, Lörrach, Germany) software with the Priven 2000 database model. The temperature dependence of the viscosity and surface tension of the model glass is shown in Figure 2. For comparison, the viscosity and surface tension of a soda-lime silicate glass and an aluminum melt were added. The curves show that the model glass had a

significantly reduced surface tension compared with the aluminum melt. However, the reduced viscosity of the model glass was still about three orders of magnitude higher than that of the aluminum melt.

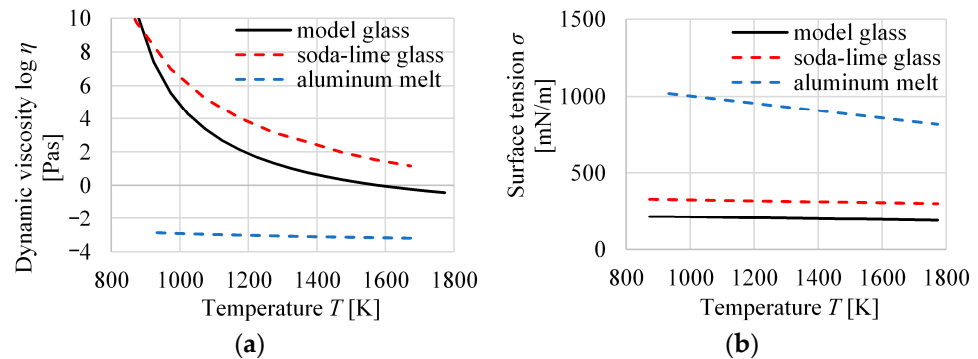


Figure 2. Viscosity and surface tension of the used model glass in comparison with a reference soda-lime glass (DGG1 standard) and aluminum melt: (a) dynamic viscosity (measured data for model glass, literature data for soda-lime glass [32] and aluminum [33]); (b) surface tension (calculated data for model glass and soda-lime glass, literature data for aluminum [34]).

Atomization experiments were carried out using the self-designed setup shown schematically in Figure 3. The glass melting unit consisted of a cylindrical tank (6.2 L) with a conical bottom outlet. It was made of platinum to ensure long service life and low contamination of the glass melt. The melt was heated indirectly by eight high temperature heating elements. The outlet temperature was controlled by inductive heating and thermocouples at the upper and lower part of the drain. The outlet orifice had an outlet diameter of 3.5 mm. The start and stop of the glass flow was controlled independently by another inductive heating loop.

The free-fall atomizer, made of heat resistant steel, was placed below the melting unit. The gas nozzles within the primary nozzle had a cumulative outlet area of 16.2 mm² and those of the secondary nozzle had a cumulative outlet area of 29.2 mm². Each outlet ring consisted of a set of semicircular holes. The outlet angles were either 5° (primary nozzle) or 15° (secondary nozzle) from the vertical. Additional details of the nozzle system are shown in Figure 4a.

The primary nozzle gas flows were controlled by conventional flow meter (Uniflux Standard S, VAF Fluid-Technik, Lichtenau, Germany), while the gas flows of the secondary nozzle were electronically controlled by mass flow controllers (MKS Instruments, type 1579 A, Andover, MA, USA). Methane 2.5 was used as the fuel gas instead of natural gas to increase reproducibility. Oxygen 2.5 was also used to allow freer adjustment of the gas mixture, and (oil-free) compressed air because of the limited control range of the oxygen supply. A fixed gas flow ratio of methane (11.8 ± 0.9 L/min), oxygen (17.9 ± 1.25 L/min) and air (7.8 ± 1.25 L/min) was used for the primary nozzle. The values were determined during pre-tests to ensure a stable process for all gas flows investigated. The flow rates used for the secondary nozzle and the melting temperatures achieved are shown in Table 1. All gas flow rates are given as standard volumetric flow rates (273.15 K, 1013.25 hPa). The melting temperatures were set to either 1533 K (low temperature, designated lt-series), or 1673 K (high temperature, designated ht-series).

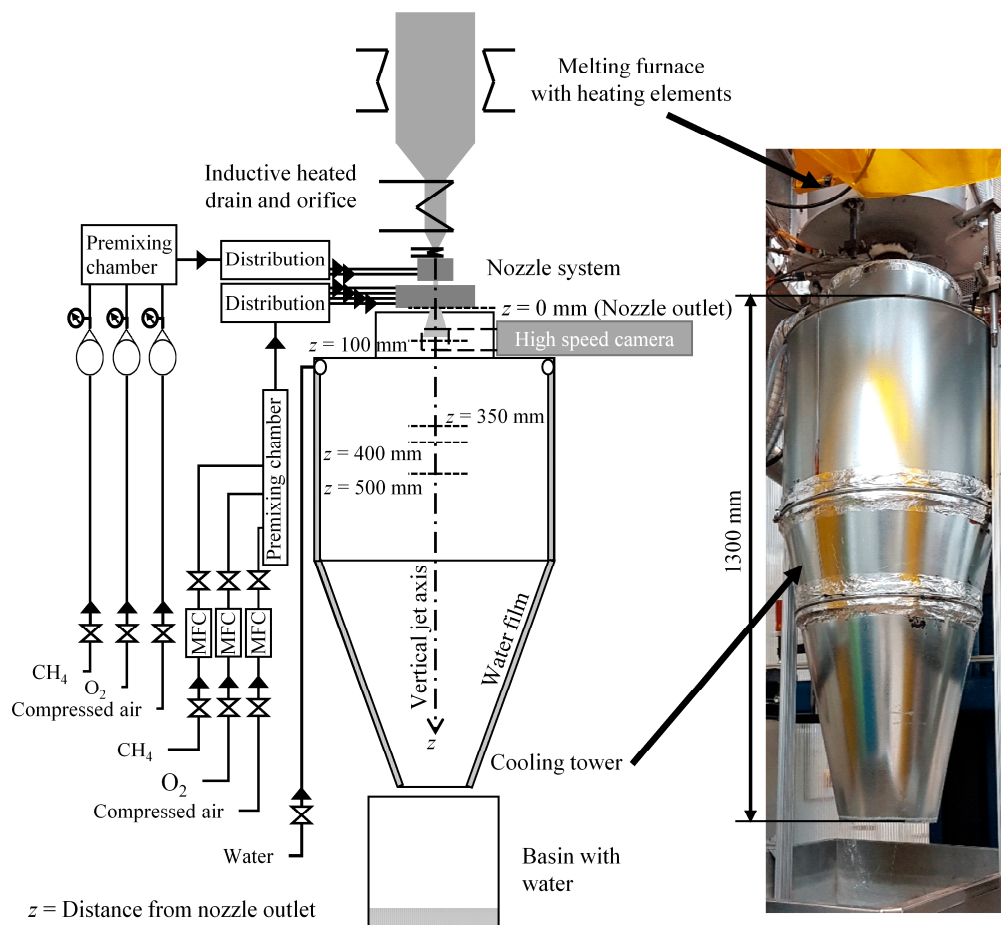


Figure 3. Schematic structure of the experimental setup left and photo on the right (drawing not in scale).

Table 1. Overview of experiments and gas flow settings.

Test Designation	Melting Temperatures		Gas Settings Secondary Nozzle			
	T_{melt} [K]	T_{drain} [K]	CH ₄ [L/min]	O ₂ [L/min]	Air [L/min]	Total [L/min]
lt_225 L/min	1533	1473	75	150	0	225
lt_255 L/min	1533	1473	75	180	0	255
lt_315 L/min	1533	1473	75	180	60	315
ht_255 L/min	1673	1523	75	180	0	255
ht_315 L/min	1673	1523	75	180	60	315

The premixed glass batch powder (1.5 kg of raw batch powder yielded about 1.1 kg molten glass) was first heated to 1373 K, and then to 1533 K or 1673 K, respectively, with a residence time of 1 h. The outlet temperature during atomization was set to 1473 K or 1523 K, respectively. The set power of the nozzle heater was 750 W.

After atomization and blowing, the melt droplets were rapidly cooled in a falling film chiller and collected in a water basin (333 K). Any hollow glass microspheres floated to the surface due to their buoyancy, allowing easy harvesting. The solid glass particles sedimented to the bottom of the water basin. During each experiment, four samples were collected within 60 s.

The solid particle samples were pre-sorted by wet sieving into three fractions: (A) greater than 4 mm, (B) 2 to 4 mm, and (C) less than 2 mm. Fraction (A) was cleaned with isopropanol to avoid adhesion. Fraction (C) was left to rest to allow any hollow glass particles to rise to

the surface. Any hollow glass bubbles were then skimmed off and collected in separating funnels. Any hollow particles from fraction C were cleaned with isopropanol, which was then evaporated, leaving behind clean and dry glass bubbles ready for scanning electron microscopy (SEM) (Evo[®] 40, Zeiss, Jena, Germany). All solid particles in fractions B and C were filtered (ROTILABO[®] filter type 601, retention range 5–13 μm , Carl Roth GmbH + Co. KG, Karlsruhe, Germany), cleaned with isopropanol and dried. The solid particles were finally classified by sieve analysis and calculation of the median particle diameter. They were also examined by light and scanning electron microscopy. To prevent inaccuracy by losses of the smallest particle sizes and an improved evaluation in this size range, the smallest sieving fraction (<125 μm) was further characterized using a particle size analyzer (CILAS[®] 1090, CILAS (3P Instruments GmbH & Co. KG), Odelzhausen, Germany).

In order to characterize the outlet temperature of the glass melt stream, additional tests were carried out using the same melting and release settings as previously described. The melt temperature at the outlet was determined by placing a sheathed thermocouple (type S) directly into the glass melt stream below the outlet of the platinum orifice at a distance of 5 mm. The thermocouple was held in a fixed position by stops to ensure a comparable temperature measurement for the different experiments.

The gas flow behavior in the area of atomization was investigated using a Prandtl probe (KIMO[®] Prandtl type L, MDUA, Münster, Germany) because of its high accuracy and reproducibility (<1% according to manufacturer). Due to the limited temperature resistance of the Prandtl probe, cold gas measurements were taken close to the nozzle, and hot gas measurements at a further distance of 350 to 500 mm (see Figure 3). The measurement point was considered to be at the tip of the probe.

A diagnostic system for flame spraying (Spraywatch 2S[®], Oseir, Tampere, Finland) was used to visualize the break-up process. The system was positioned approximately 100 mm below the nozzle to visualize the disintegrated glass melt. The radial distance from the vertical nozzle axis was 210 mm due geometrical limitations. The monitored area was 22 mm wide, and 29.5 mm high. The depth of focus was approximately 2.2 mm. The shutter speed was 5 μs .

Non-measurable parameters such as the gas velocity in the atomization zone were calculated using numerical simulations. The fluid dynamics of the combustion process without melt flow was calculated using the commercial software Simcenter STAR-CCM+[®] (v. 2022.1.1, Siemens, Munich, Germany), which uses the finite volume method. The built-in “complex chemistry” model with laminar flamelet method was used for the combustion reaction. The reaction mechanism of methane combustion was implemented in STAR-CCM+[®], referencing the work of Lu and Law [35]. The fluid flow was calculated using a segregated flow model for calculating pressure and velocity field with ideal gas behavior. The turbulence was modeled by the Reynolds-averaged Navier–Stokes equations, applying the κ - ϵ turbulence model. The gas viscosity was calculated internally by STAR-CCM+[®] as a function of local combustion gas composition and temperature according to Sutherland law, and the ideal gas law was used to express density as a function of temperature and pressure. The inlet conditions were set to be equivalent to the experimental conditions in terms of gas composition (CH_4 , O_2 , N_2) and mass flow rates and an inlet temperature of 300 K. For the gas inlet, the mass flow boundary condition was used. For the boundary conditions of the gaseous volume to the environment, the pressure was set to environmental pressure. The outer boundaries of the solid steel body of the nozzle system fulfilled an external heat flux condition of $4 \text{ W} \cdot \text{m}^{-2} \text{K}^{-1}$ to account for heat loss to the environment.

Finally, the symmetry of the nozzle system was used to reduce the computation time by applying a 3D half model consisting of about 877,700 cells. A polyhedral mesher with a base cell size of 5 mm for the solid parts of the burner and 2.5 mm for the coarse part of the gaseous volume was used. For the refined part in the center of the model, a base cell size of 0.5 μm was applied. At the interface to the solid parts, the prism layer mesh was applied. The meshed model is shown in Figure 4b. Figure 4c shows an example of the calculated gas velocity distribution of the flame region for a gas flow rate of 225 L/min.

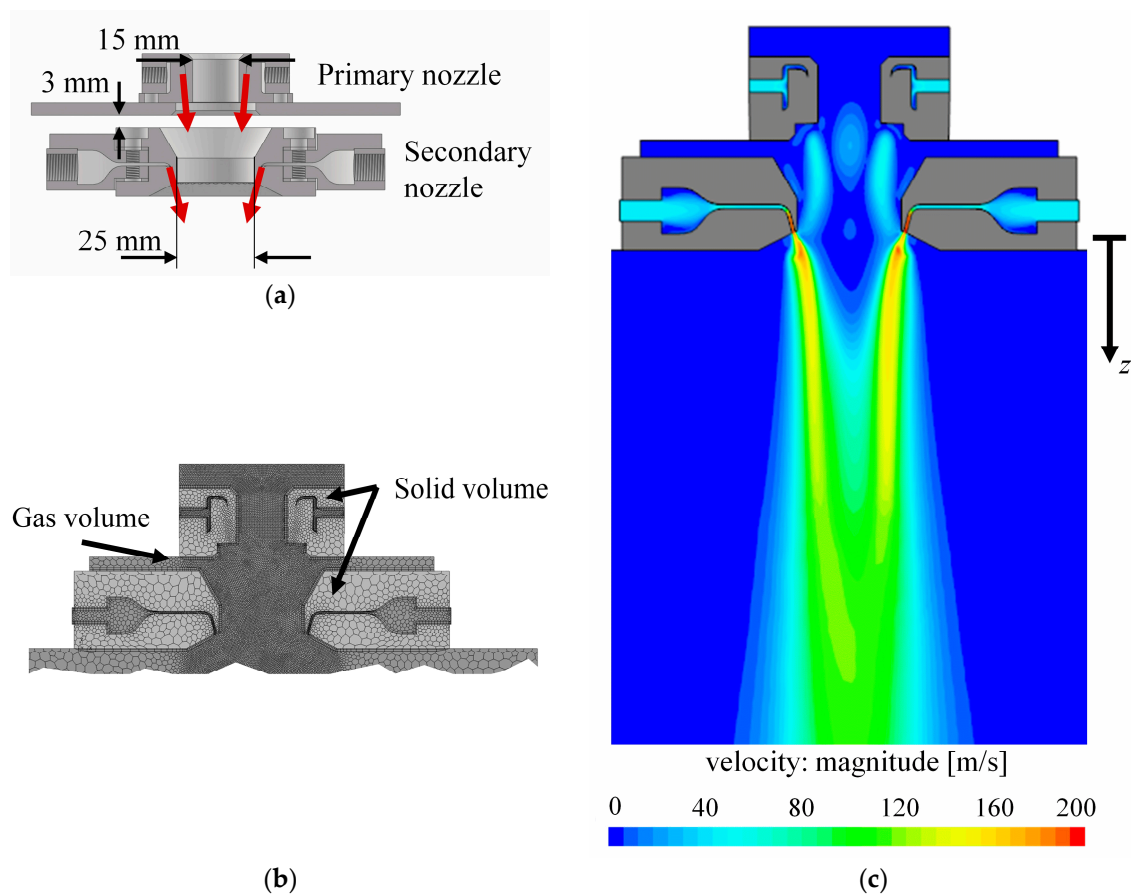


Figure 4. Sketch of free-fall atomizer: (a) CAD model of the designed nozzle system (sectional view); (b) simplified, meshed CFD model for simulation; (c) simulated gas velocity distribution within the flame region at a gas inlet rate of 225 L/min.

3. Results

The results of the numerical simulation of the gas velocity along the vertical jet axis are plotted in Figure 5 for different gas flow rates. The curves in Figure 5a are calculated without gas combustion, while those in Figure 5b include gas combustion. The plotted values are obtained by integrating the gas velocities within a radial distance of 5 mm from the vertical jet axis at each individual axial position. This procedure was designed to account for flow instabilities that typically lead to melt jet deviations and provide a smoothed range of values.

The simulation without combustion showed a maximum velocity at an axial distance in the range of 55 mm to 65 mm from the nozzle (see Figure 5a), independent of the gas flow rate. With combustion included, the calculated velocities increased as expected from about 40...55 m/s to about 130...170 m/s, reaching a maximum velocity at about 80...90 mm distance from the nozzle (see Figure 5b). The point of maximum velocity is considered to be the starting point of atomization. The flow and temperature conditions at this axial position were used as a reference point for further considerations and data analysis. The calculated temperature profiles along the vertical jet axis are shown in Figure 5c. The maximum temperatures were in the range of 3000 K. With increasing gas flow rate, the temperature decrease along the jet axis was more pronounced. For example, the gas phase temperature dropped below the required blowing temperature of 1673 K at 225 L/min after a distance of $z = 420$ mm, and at 315 L/min after $z = 320$ mm, respectively.

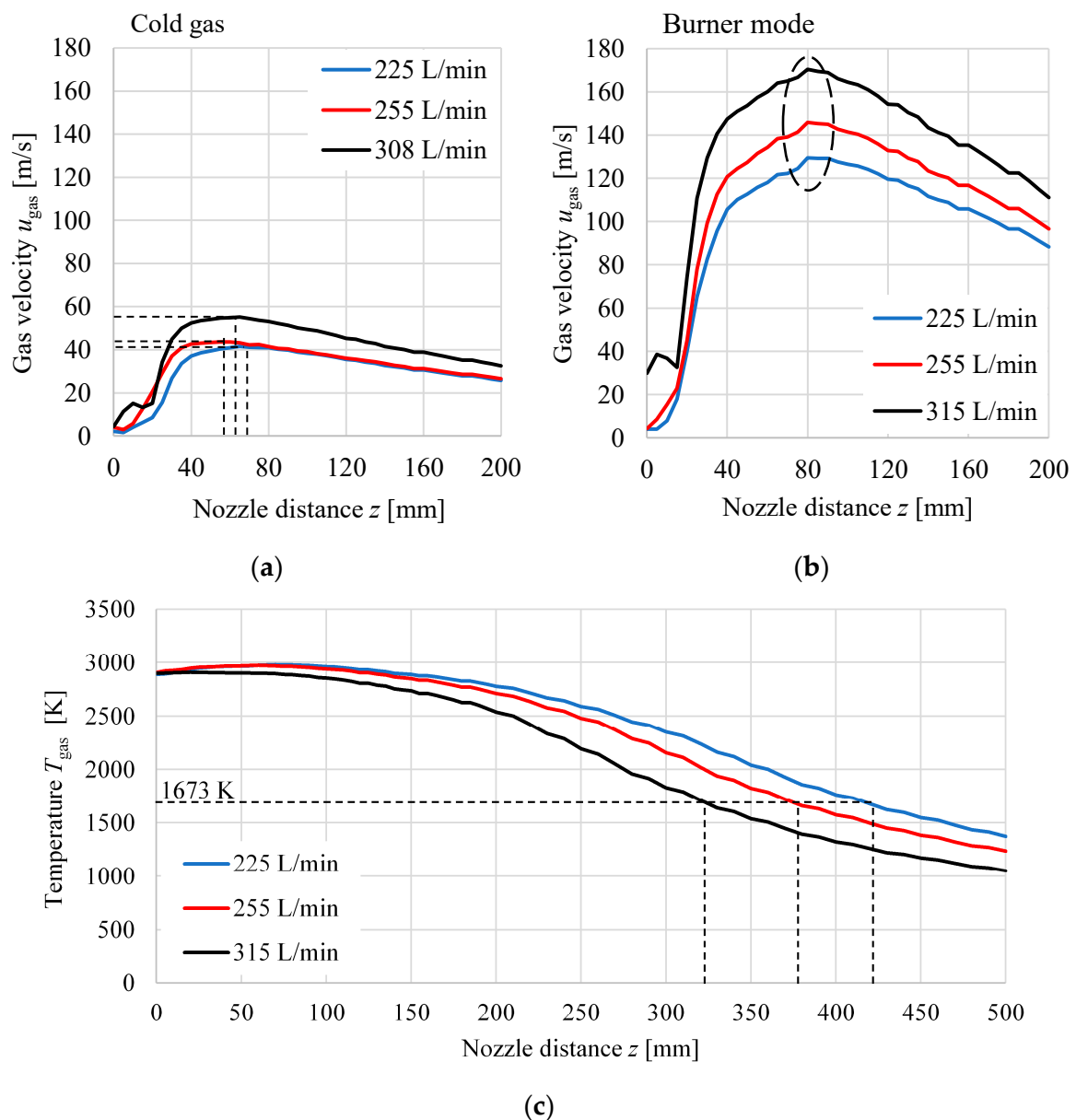


Figure 5. Calculated gas velocities from CFD simulation for different gas flows: (a) cold gas conditions without combustion model; (b) hot gas conditions with combustion model. The starting point of atomization is assumed to be in the highlighted area at nozzle distance of about 80 mm; (c) calculated temperature profile along vertical jet axis with activated combustion model.

To validate the CFD model, the calculated radial velocity distributions for cold gas conditions (i.e., without combustion) are compared in Figure 6a,b with the velocity measurements obtained with the Prandtl probe close to the nozzle ($z = 100 \dots 150$ mm). The flow rates were 225 L/min and 308 L/min, respectively. In Figure 6a, the calculated peak velocities around $r = 0$ mm were in good agreement with experimental results, while the experimental data deviated by about ± 5 m/s along the rising and falling edges of the velocity profiles. The agreement between calculation and experiment improved at a gas flow rate of 308 L/min, as shown in Figure 6b.

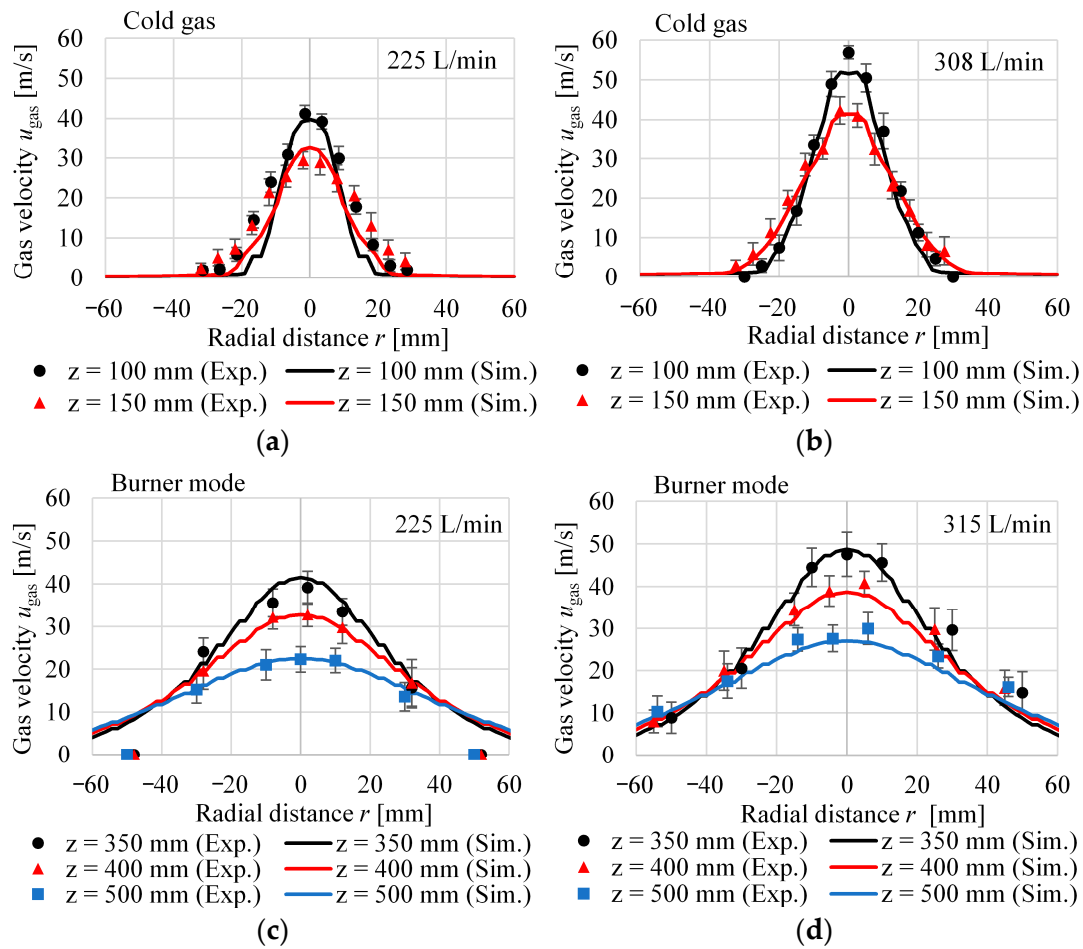


Figure 6. Calculated gas velocity and comparison with experimental data. Horizontal profiles of cold gas measurement: (a) 225 L/min; (b) 308 L/min. Simulation and measurement of burner mode: (c) 225 L/min; (d) 315 L/min.

The comparison of measured and calculated gas velocities under hot gas conditions is shown in Figure 6c,d. Due to the limited operating temperature of the Prandtl probe, the measurement was performed at a greater distance from the nozzle ($z = 350 \dots 500$ mm). Under hot gas conditions, a satisfying agreement between calculated and measured gas velocities was obtained for both gas flows at these distances. Therefore, we considered the CFD model to be acceptably valid for both cold and hot gas conditions, making it useful for further data analysis and consideration.

Except for the total gas mass flow, \dot{m}_g , which was used as a boundary condition in the simulation model, all property values in Table 2 for the gas phase were obtained from simulation data sets at the assumed atomization area at the axial position $z = 80$ mm (cf. Figure 5b). The mass flow of the gas, \dot{m}_g , is the sum of the two gas flows from the primary and secondary nozzle. The values of the gas properties are summarized in Table 2.

Table 2. Properties of the gas phase at different gas flow rates in the atomization area.

Test Designation	u_g [m/s]	\dot{m}_g [kg/s] $\times 10^{-3}$	T_g [K]	ρ_g [kg/m ³]	η_g [Pas] $\times 10^{-5}$	ν_g [m ² /s] $\times 10^{-4}$
lt_225 L/min	129.5	5.21	2976	0.093	7.98	8.58
lt_255 L/min	145.9	5.91	2962	0.097	7.76	8.00
lt_315 L/min	170.4	7.22	2873	0.106	7.83	7.38
ht_255 L/min	145.9	5.91	2962	0.097	7.76	8.00
ht_315 L/min	170.4	7.22	2873	0.106	7.83	7.38

As described above, the temperature-dependent properties of the glass melt were either based on measurements (temperature or viscosity) or were obtained using the SciGlass[®] Professional (v. 7.11) software. Table 3 gives an overview of the melt properties considered at the point of atomization. The deviations of the listed melt temperatures corresponded to the changes in the measured outlet temperature during the separate tests. The density of the glass melt, ρ_1 , was assumed to be approximately constant (2300 kg/m^3). The diameter of the melt flow, d_1 , was derived from photographs as shown in Figure 7a.

Table 3. Measured and calculated properties of the glass melt.

Test Designation	u_1^\diamond [m/s]	\dot{m}_1 [kg/s] $\times 10^{-3}$	d_1^* [mm]	T_1^* [K]	η_1^* [Pas]	ν_1^\diamond [m ² /s] $\times 10^{-4}$	σ_1^\diamond [N/m]
lt_225 L/min	0.60	1.56 ± 0.07	1.2 ± 0.1	1485 ± 8	2.03	8.83	0.198
lt_255 L/min	0.67	1.75 ± 0.12	1.2 ± 0.1	1485 ± 8	2.03	8.83	0.198
lt_315 L/min	0.72	1.87 ± 0.05	1.2 ± 0.1	1485 ± 8	2.03	8.83	0.198
ht_255 L/min	0.46	2.41 ± 0.11	1.7 ± 0.1	1567 ± 10	1.11	4.83	0.195
ht_315 L/min	0.45	2.36 ± 0.18	1.7 ± 0.1	1567 ± 10	1.11	4.83	0.195

* measured, \diamond calculated.

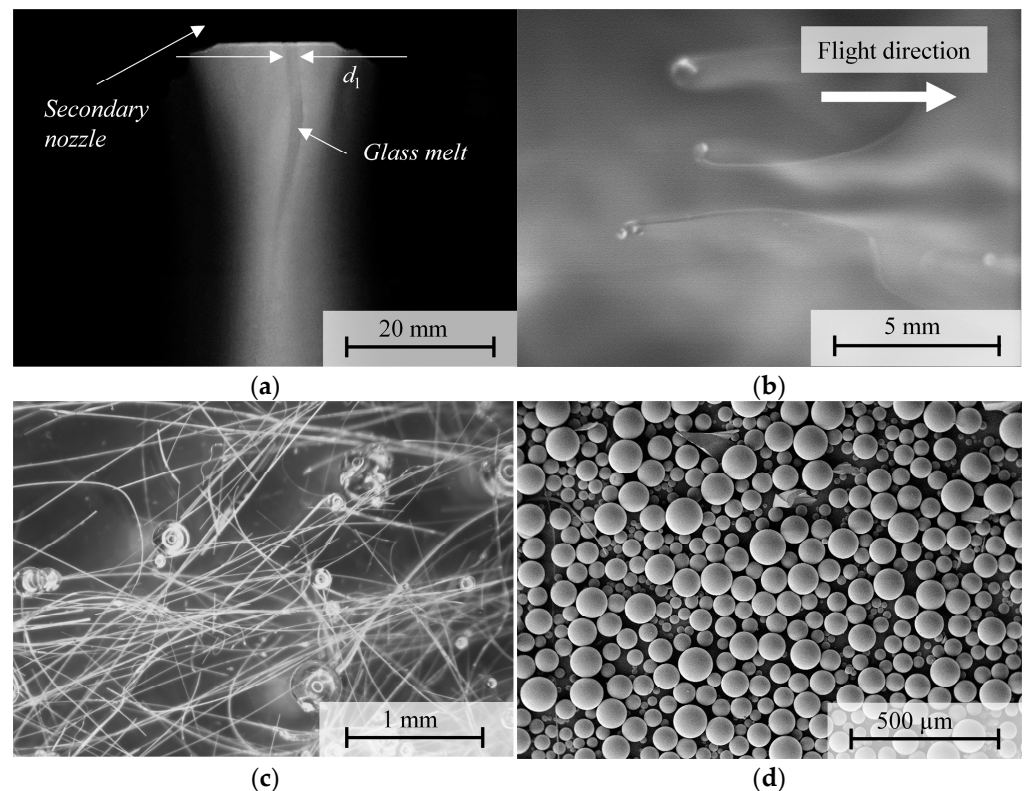


Figure 7. Images during and after atomization: (a) image of the glass melt leaving the secondary nozzle; (b) image of the disintegrated glass melt during the experiment lt_255 L/min; (c) light microscope image of separated fiber fraction (>4 mm), and (d) SEM image of separated solid particles with diameters < 125 μm .

Figure 7a,b was taken during atomization experiments. Figure 7a is a photograph of the glass melt leaving the secondary nozzle. Although it was subject to instabilities and disturbances, it was not disrupted. Figure 7b shows an image taken by the Spraywatch instrument at a gas flow rate of 255 L/min (lt_255 L/min). Here, the glass melt has passed the breakup point and was being broken into ligaments and droplets. Due to the limited resolution, only the larger particles are visible. Figure 7c shows a light microscope image of a sample fraction containing a high proportion of fibers, some of which have a shape

similar to the head–tail features observed in Figure 7b. Finally, Figure 7d finally shows a collection of solidified droplets collected in particle fraction (C). Their shape is almost perfectly spherical.

The results of the atomization experiments in terms of particle size distribution are illustrated in Figure 8. Figure 8a,b shows the results of sieve analysis of the solid particles that sedimented in the quench. Firstly, a shift towards smaller particle size was observed with increasing gas flow rate for both the low temperature (lt) and high temperature (ht) series. The mass of small particles (<125 μm) increased from 2.3 wt% to 7.3 wt% in the lt-series, while up to 9 wt% were achieved in the ht-series at 315 L/min.

As described above, the smallest particle fraction was additionally characterized using a CILAS particle analyzer (Figure 8c,d). Here all experiments showed almost the same size distribution. The majority of the particles smaller than 125 μm had a diameter greater than 20 μm and the median diameter was in the range from 80 μm to 90 μm .

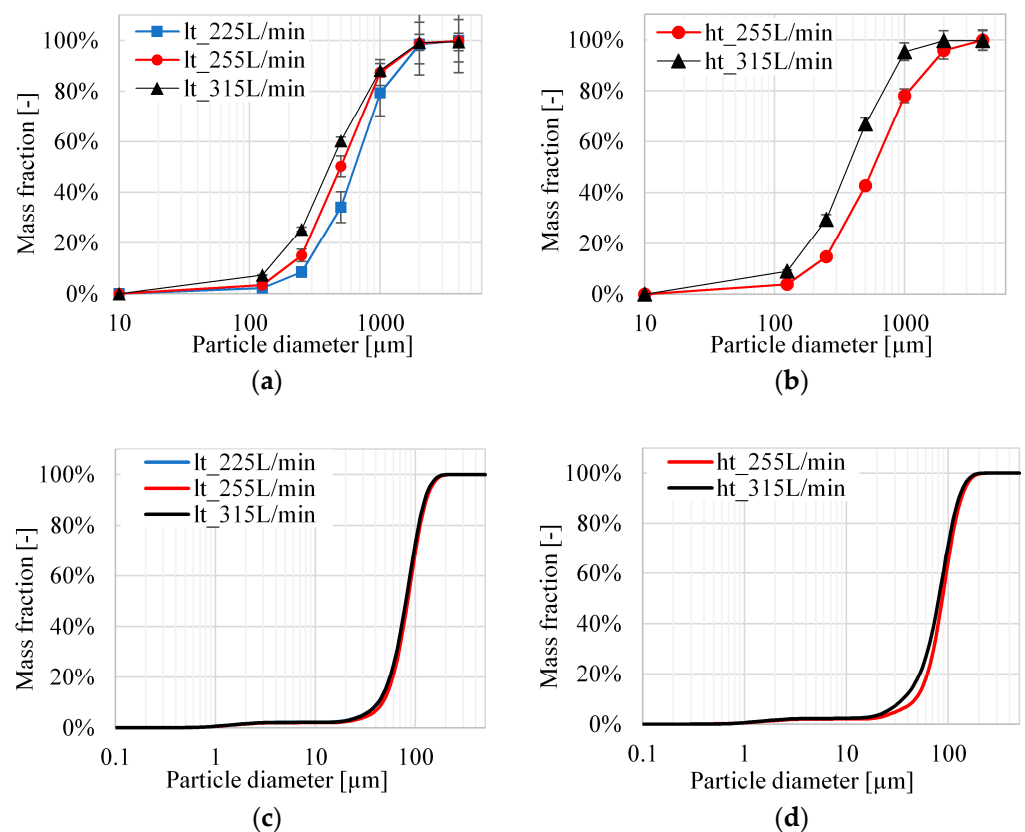


Figure 8. Size distribution of quenched solid particles determined by sieving analysis: (a) low-temperature tests (lt); (b) high-temperature tests (ht). Size distribution of the size fraction < 125 μm determined by means of particle size analyzer (CILAS® 1090): (c) lt-series; (d) ht-series.

The measured median diameters $d_{50,3}$ of all particles are plotted in Figure 9a as a function of the relative Weber number $We_{g,rel}$. As expected, the median particle sizes decreased with increasing $We_{g,rel}$ for each test series: from 637 μm to 410 μm in lt-series, and from 575 μm to 366 μm in ht-series. Contrary to particle size, the amount of fibers increased with increasing Weber number (Figure 9b).

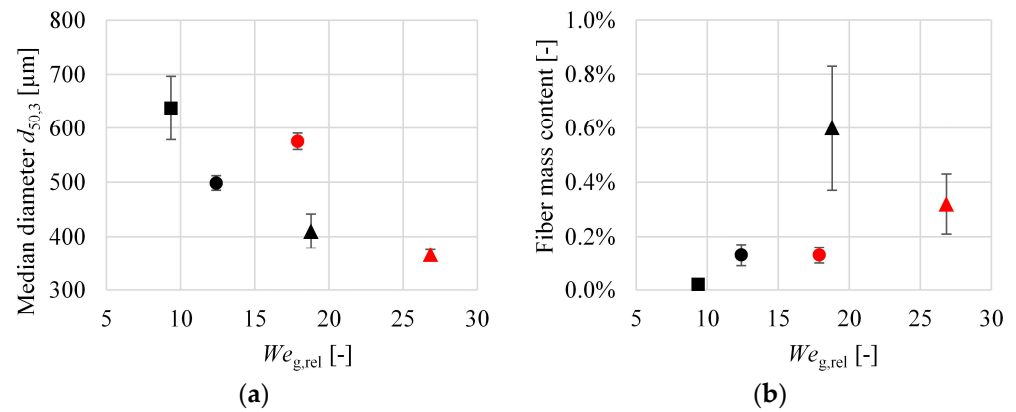


Figure 9. Relation between the relative gas Weber number, $We_{g,rel}$, and experimentally determined parameters while using the following gas flow rates: ■ 225 L/min, ● 255 L/min, ▲ 315 L/min; black markers, lt-series; red markers, ht-series; (a) median particle diameter $d_{50,3}$; (b) fiber content.

The Weber number for the gas and liquid phase and the gas mass ratio (GMR) were calculated from Equations (3), (5) and (7) from the values given in Tables 2 and 3. The results are summarized in Table 4.

Table 4. Measured and calculated parameters of the atomization experiments.

Test Designation	$We_{g,rel}$ \blacklozenge [-]	$We_{l,rel}$ \blacklozenge $\times 10^5$ [-]	GMR \blacklozenge [-]	Median Diameter $d_{50,3}$ * μm	Fiber Content * [wt%]
lt_225 L/min	9.4 ± 2.1	2.31	3.34 ± 0.18	637.3 ± 59.0	0.02 ± 0.02
lt_255 L/min	12.4 ± 2.5	2.94	3.38 ± 0.25	498.5 ± 13.3	0.13 ± 0.04
lt_315 L/min	18.8 ± 3.8	4.08	3.86 ± 0.16	410.3 ± 31.5	0.60 ± 0.23
ht_255 L/min	17.9 ± 3.7	4.24	2.46 ± 0.13	575.3 ± 15.1	0.13 ± 0.03
ht_315 L/min	26.8 ± 5.5	5.82	3.06 ± 0.25	366.0 ± 9.5	0.32 ± 0.11

* measured, \blacklozenge calculated.

Over 99 wt% of the particles sedimented in the quench, with only a few (<0.1 wt%) light spheres found floating on the surface. After separation from water and cleaning with isopropanol, these floating spheres were dried. The SEM image in Figure 10a shows separated hollow glass bubbles. Predominantly, the diameters of the bubbles were up to $50 \mu\text{m}$ and had almost perfect spherical shapes. Figure 10b shows a close-up view of hollow spheres broken during preparation with wall thicknesses in the range of less than, or equal to, $1 \mu\text{m}$.

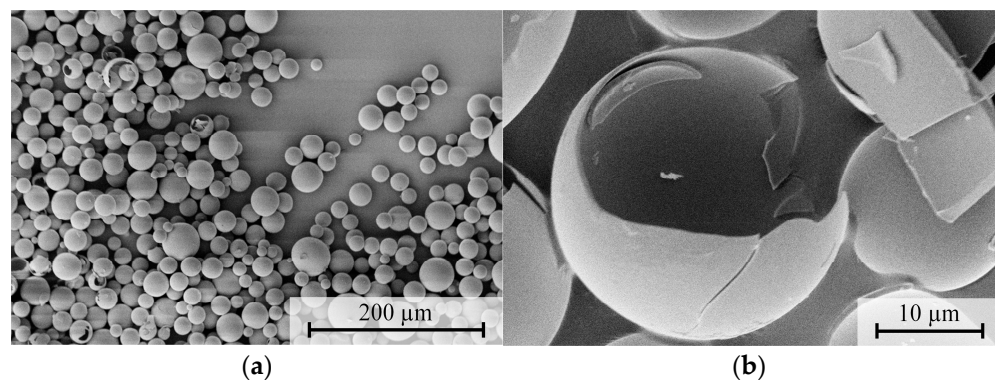


Figure 10. SEM image of floatable hollow glass microspheres: (a) overview; (b) detailed image of a shattered hollow glass sphere with a diameter of about $20 \mu\text{m}$ and a wall thickness of less than $1 \mu\text{m}$.

4. Discussion

The results of the study showed that complete disintegration of the borosilicate glass melt was achieved. Over 99% by weight of the melt flow formed into glass droplets. The mean diameter of atomized particles ranged from 366 μm to 637 μm . Primarily, the gas flow rates or gas velocities controlled the film break-up, as shown by the influence of $We_{g,rel}$ number in Figure 9a, in accordance with the mathematical expression in Equation (6), which describes the influence of relevant parameters on atomization. Contrary to expectations, increasing the melt temperature did not result in significantly smaller melt droplets due to the reduced viscosity and surface tension of the glass melt. Instead, the droplet size partly increased in the ht-series. This can be explained by the simultaneous increase in melt flow at higher melt temperatures (see Table 3), which leads to a lower gas mass ratio (GMR) according to Equation (7). Consequently, the GMR has a greater influence on droplet size than the reduced viscosity and surface tension of the melt, i.e., melt outflow is influenced by the coupling of several parameters.

The identification and determination of the relevant process parameters (see Tables 3 and 4) was achieved by a combination of measurements and simulations. The results showed that the simulations including the combustion process reached higher maximum gas velocities in the symmetry line, in comparison with the cold gas simulation. This could be explained by the expansion of the gas volume due to the temperature rise and the resulting extended region of high gas velocities.

The identified gas and melt flow parameters allowed the calculation of the expected median diameter according to Equation (6). A comparison of the measured and calculated $d_{50,3}$ values is shown in Figure 11. The empirical parameter C in Equation (6) was obtained by least square fitting of calculated to experimentally determined $d_{50,3}$ values, resulting in $C \approx 204$. The goodness-of-fit for the linear regression is expressed as $R^2 = 0.9859$. The results showed an acceptable agreement between calculated and measured median diameters. The determined value of parameter C was higher than reported for atomization of metal melts ($C = 40 \dots 50$) [12,26] but lower than reported for mineral melts ($C = 240$) [12].

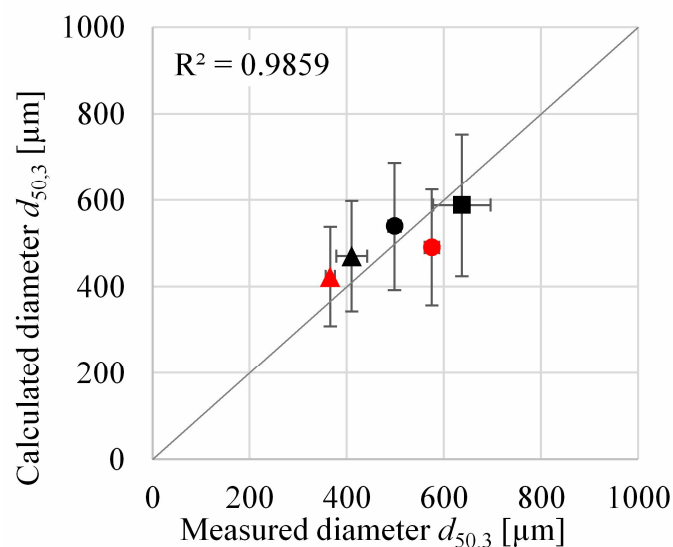


Figure 11. Comparison of measured and calculated median particle diameter according to Equation (6) with the fitting parameter, $C = 204$; ■ 225 L/min, • 255 L/min, ▲ 315 L/min; black markers, data points of lt-series; red markers, data points of ht-series.

A broad particle size distribution of the atomized glass melt was found to be characteristic of the experiments performed with the free-fall atomizer. In comparison with metal melts, the glass melt used showed a strong temperature dependence of viscosity—even though the model glass developed turned out to be a low-viscosity glass.

A look at the Weber numbers achieved in Table 4 shows that $We_{g,rel}$ only exceeded 25 in one test, resulting in a mean diameter of 366 μm . To improve the atomization and reduce the median particle diameter, an increase in Weber number should be achieved. For example, based on the results obtained, a $We_{g,rel} = 50$ could be achieved with a relative gas velocity of approximately 300 m/s; this would give a median particle size of approximately 250 μm . Moreover, $We_{g,rel} = 100$ could be achieved with a relative velocity of about 410 m/s, giving a median diameter of 175 μm .

A small portion of less than 1% by weight of the atomized melt formed glass fibers during the process (see Table 4). The reason for fiber formation is the relatively high viscosity and low surface tension of glass melts compared with metal melts such as aluminum (see Figure 2). During break-up, stretched primary ligaments are formed (see Figure 7b) [30]. If such ligaments unintentionally leave the hot zone of the burner flame too early, these ligaments will easily solidify and form fibers because the viscosity of the glass melt increases rapidly by several orders of magnitude with decreasing temperature (compare Figure 2). With increasing gas flow rates, the amount of fibers increase (Figure 9b) as more melt ligaments leave the hot zone due to higher gas velocities and presumably lower flame temperatures as the fuel/oxygen ratio decreases (see Tables 1 and 2). In contrast, the amount of fibers decreases at higher melt temperature (Figure 9b) due to the decrease in melt viscosity. Nevertheless, fiber formation is well controlled, and hot gas atomization improves the roundness of the glass droplets [12,28,30].

The formation of hollow glass microspheres during the process was also achieved. However, only a small mass fraction of less than 0.1 wt% glass droplets had formed hollow glass spheres. The hollow glass bubbles found had diameters up to 50 μm and a wall thickness of less than or equal to 1 μm . Assuming conservation of mass, the original droplet size before blowing should have been about 25 μm or less. Measurement of the particle size distribution of the fraction < 125 μm showed that only 3 to 5 wt% of the particles were smaller than 25 μm (see Figure 8c,d). With respect to the total mass of atomized glass particles, the percentage of droplets < 25 μm was between 0.1 wt% and 0.5 wt%, depending on the gas flow. As discussed above, reducing the median droplet size would result to a higher number of <25 μm droplets. Therefore, a higher number of hollow microspheres would be expected as the Weber number increases. However, as gas velocities or Weber numbers increase, detrimental turbulence and instability can be expected. This can be a limiting factor in the atomization process, and to prevent this, appropriate adjustments to stabilize the process will be necessary. Another limiting factor could be the high viscosity, compared with other fluids or melts, which inhibits the atomization process.

The reason that only the smallest particles were blown into hollow spheres is also related to the limitation of residence time and heat transfer within the hot zone, which provides sufficient temperatures for blowing ($T > 1673$ K). The length of the hot zone is approximately 240 mm to 340 mm from the assumed atomization point ($z = 80$ mm) as shown in Figure 5c. Assuming a maximum vertical jet velocity of about 130 m/s to 170 m/s, theoretically the minimum residence time in the hot zone is 1.5 to 2.5 milliseconds. Increasing the residence time could facilitate the expansion of even larger droplets, thus increasing the total amount of hollow microspheres.

Although free-fall atomizers are commonly used for atomizing glass melts, alternative concepts are being considered to achieve a higher yield of hollow glass spheres. For example, close-coupled atomizers or ultrasonic wave atomizers could be used to achieve higher impact for break-up [12]. Another alternative is prefilming atomization which aims at pre-thinning the melt through rotational forces, where one dimension can be reduced to the required dimension of few micrometers [36]. These variants will be considered for future approaches.

5. Conclusions

For the first time, a free-fall atomizer process for direct atomization of a glass melt stream in combination with in-situ blowing of the solid droplets into hollow glass micro-

spheres has been achieved. The production of hollow glass microspheres was successfully demonstrated for small melt droplets.

Atomization of glass melts requires both high temperatures and high impact. Therefore, a free-fall atomizer was developed comprising a high-performance burner to achieve high gas velocities. The burner nozzle produced gas velocities of up to 170 m/s and a gas phase temperature of up to 3000 K in the disintegration region. The point of atomization was found to be approximately 80 mm below the nozzle. The length of the subsequent hot zone for blowing the glass droplets into hollow spheres at temperatures above 1673 K was between 240 mm and 340 mm. The glass melt was successfully broken into droplets: 99 wt% of the melt formed into droplets and 1 wt% formed into fibers. Depending on the process parameters, the mean value of the droplet diameters was between 366 μm and 637 μm and showed good agreement with calculated values obtained using an empirical equation for the atomization of metal melts.

Overall, the droplet size ranged from about 2 μm to 4 mm, showing that the free-fall atomizer produced a wide droplet size distribution. The droplet size decreased significantly as the Weber number increased, due to the increase in gas velocity, and hence the higher impact on melt breakup. However, although a low-viscous glass melt with low surface tension was developed for the trials, the majority of the particles were greater than 125 μm . The formation of sufficiently small droplets for blowing microspheres is, therefore, limited.

Hollow glass spheres with diameters up to 50 μm and wall thickness of equal or less than 1 μm were found. Considering the conservation of mass, the atomized, pre-blown melt droplets had diameters of about 25 μm or smaller. Analysis of the smallest particle fraction showed that less than 0.5 wt% of all droplets met this requirement. Of this fraction, a maximum of 20 wt% was blown into hollow glass spheres.

In order to achieve higher yields of small droplets, the Weber number could be increased to achieve a higher instability of the melt stream, followed by a more effective disintegration, but probably at the expense of a higher fibers content. On the other hand, an extension of the hot zone could provide longer residence times for sufficient blowing of even larger melt droplets after atomization. Further improvements for the production of hollow microspheres could be achieved by alternative atomization principles such as prefilming of the liquid melt. To investigate this, an adapted system will be considered where one dimension is reduced to the required size by prefilming and then atomized into small droplets. Another approach will be the reduction in the viscosity by increasing the amount of alkali oxides to improve the atomization efficiency. Overall, in situ production of hollow glass spheres by melt atomization is a promising way to increase energy efficiency compared with current state of the art techniques and will be further investigated.

Author Contributions: Conceptualization, T.H., A.R. and T.G.; methodology, T.H.; software, T.H. and A.R.; validation, T.H., F.R. and A.R.; investigation, T.H. and A.R.; resources, T.H.; data curation, T.H.; writing—original draft preparation, T.H. and A.R.; writing—review and editing, F.R., A.R. and T.G.; visualization, T.H.; supervision, W.K. and T.G.; project administration, T.G. All authors have read and agreed to the published version of the manuscript.

Funding: This research was funded by Bundesministerium für Bildung und Forschung (13FH132PX8) of the program “FHprofUnt 2018” and the project partner Franken Maxit GmbH, Füller Glastechnologie-Vertriebs GmbH and 3M/Dyneon GmbH. The APC was funded by the Bavarian Ministry of Science and Art/Deggendorf Institute of Technology.

Data Availability Statement: The data that support the findings of this study are available from the corresponding author, T.H., upon reasonable request.

Acknowledgments: Additional thanks to Zentrum für Glas- und Umweltanalytik Ilmenau GmbH for measuring the glass viscosities. Further thanks to M. Paternoster for the technical support during the experimental implementation.

Conflicts of Interest: The authors declare no conflict of interest. The funders had no role in the design of the study; in the collection, analyses, or interpretation of data; in the writing of the manuscript; or in the decision to publish the results.

References

1. Bobkova, N.M.; Savchin, V.V.; Trusova, E.E.; Pavlyukevich, Y.G. Rheological Basis of Hollow Glass Microsphere Production Based on Alkali-Borosilicate Systems. *Glass Ceram.* **2018**, *75*, 3–6. [CrossRef]
2. Bobkova, N.M.; Trusova, E.E.; Savchin, V.V.; Sabadakha, E.N.; Pavlyukevich, Y.G. Obtaining Hollow Glass Microspheres and Their Use in the Production of Water-Dispersion Coatings. *Glass Ceram.* **2020**, *76*, 401–405. [CrossRef]
3. Karasu, B.; Demirel, İ.; Öztuvan, A.; Özdemir, B. Glass Microspheres. *El-Cezeri Fen Mühendislik Derg.* **2019**, *6*, 613–641. [CrossRef]
4. 3M Advanced Materials Division. Start Something Big, by Thinking Small: 3M®Glass Bubbles. Available online: <https://multimedia.3m.com/mws/media/10283300/3m-glass-bubbles-overview.pdf> (accessed on 8 May 2022).
5. Beck, W.R.; O'Brien, D.L. Glass Bubbles Prepared by Reheating Solid Glass Particles. U.S. Patent US3365315A, 23 August 1963.
6. Veatch, F.; Alford, H.E.; Croft, R.D. Method of Producing Hollow Glass Spheres. U.S. Patent US2978339A, 22 October 1957.
7. Min'ko, N.I.; Binaliev, I.M. Role of sodium sulfate in glass technology. *Glass Ceram.* **2013**, *69*, 361–365. [CrossRef]
8. Franke, M.; Schlicke, J. Method and Device for Producing Hollow Glass Spheres. WIPO Patent WO2015110621A1, 26 January 2015.
9. Schlicke, J.; Stache, L. Method and Device for Producing Hollow Microglass Beads. WIPO Patent WO2018001409, 12 June 2017.
10. Mi, J.; Grant, P.S.; Fritsching, U.; Belkessam, O.; Garmendia, I.; Landaberea, A. Multiphysics modelling of the spray forming process. *Mater. Sci. Eng. A* **2008**, *477*, 2–8. [CrossRef]
11. Dumouchel, C. On the experimental investigation on primary atomization of liquid streams. *Exp. Fluids* **2008**, *45*, 371–422. [CrossRef]
12. Lohner, H. *Zerstäuben von Mineralschmelzen mit Heißgas*; VDI-Verl.: Düsseldorf, Germany, 2003; ISBN 3-18-376503-9.
13. Bauckhage, K. Das Zerstäuben metallischer Schmelzen. *Chem. Ing. Tech.* **1992**, *64*, 322–332. [CrossRef]
14. Hede, P.D.; Bach, P.; Jensen, A.D. Two-fluid spray atomisation and pneumatic nozzles for fluid bed coating/agglomeration purposes: A review. *Chem. Eng. Sci.* **2008**, *63*, 3821–3842. [CrossRef]
15. Minakov, A.V.; Shebeleva, A.A.; Strizhak, P.A.; Chernetskiy, M.; Volkov, R.S. Study of the Weber number impact on secondary breakup of droplets of coal water slurries containing petrochemicals. *Fuel* **2019**, *254*, 115606. [CrossRef]
16. Der, O.; Bertola, V. An experimental investigation of oil-water flow in a serpentine channel. *Int. J. Multiph. Flow* **2020**, *129*, 103327. [CrossRef]
17. Mlkvik, M.; Stähle, P.; Schuchmann, H.P.; Gaukel, V.; Jedelsky, J.; Jicha, M. Twin-fluid atomization of viscous liquids: The effect of atomizer construction on breakup process, spray stability and droplet size. *Int. J. Multiph. Flow* **2015**, *77*, 19–31. [CrossRef]
18. Li, D. *Encyclopedia of Microfluidics and Nanofluidics*; Springer: Boston, MA, USA, 2008; ISBN 978-0-387-32468-5.
19. Zhao, H.; Liu, H. Breakup Morphology and Mechanisms of Liquid Atomization. In *Environmental Impact of Aviation and Sustainable Solutions*; Agarwal, R.K., Ed.; IntechOpen: London, UK, 2020; ISBN 978-1-83962-357-8.
20. Varga, C.M.; Lasheras, J.C.; Hopfinger, E.J. Initial breakup of a small-diameter liquid jet by a high-speed gas stream. *J. Fluid Mech.* **2003**, *497*, 405–434. [CrossRef]
21. Faeth, G.; Hsiang, L.-P.; Wu, P.-K. Structure and breakup properties of sprays. *Int. J. Multiph. Flow* **1995**, *21*, 99–127. [CrossRef]
22. Chaussonnet, G.; Braun, S.; Wieth, L.; Koch, R.; Bauer, H.-J.; Sängler, A.; Jakobs, T.; Djordjevic, N.; Kolb, T. SPH Simulation of a Twin-Fluid Atomizer Operating with a High Viscosity Liquid. In Proceedings of the 13th Triennial International Conference on Liquid Atomization and Spray Systems, Tainan, Taiwan, 23–27 August 2015.
23. Lasheras, J.C.; Hopfinger, E.J. Liquid Jet Instability and Atomization in a Coaxial Gas Stream. *Annu. Rev. Fluid Mech.* **2000**, *32*, 275–308. [CrossRef]
24. Markus, S.; Fritsching, U.; Bauckhage, K. Jet break up of liquid metal in twin fluid atomisation. *Mater. Sci. Eng. A* **2002**, *326*, 122–133. [CrossRef]
25. Sängler, A.D. *Zerstäubung Hochviskoser Fluide bei Variierendem Systemdruck—Grundlagenforschung zur Hochdruck-Flugstromvergasung*; Karlsruher Institut für Technologie: Karlsruhe, Germany, 2018.
26. Lubanska, H. Correlation of Spray Ring Data for Gas Atomization of Liquid Metals. *JOM* **1970**, *22*, 45–49. [CrossRef]
27. Urionabarrenetxea, E.; Avello, A.; Rivas, A.; Martín, J.M. Experimental study of the influence of operational and geometric variables on the powders produced by close-coupled gas atomisation. *Mater. Des.* **2021**, *199*, 109441. [CrossRef]
28. Lohner, H.; Czisch, C.; Schreckenberger, P.; Fritsching, U.; Bauckhage, K. Atomization of viscous melts. *Atomiz. Spr.* **2005**, *15*, 169–180. [CrossRef]
29. Si, C.; Zhang, X.; Wang, J.; Li, Y. Design and evaluation of a Laval-type supersonic atomizer for low-pressure gas atomization of molten metals. *Int. J. Miner Metall. Mater.* **2014**, *21*, 627–635. [CrossRef]
30. Huang, Z.; Czisch, C.; Schreckenberger, P.; Büllsfeld, F.; Fritsching, U. Technical Note: Powder Production by Gas Atomization of Bioglass Melt. *Part. Part. Syst. Charact.* **2005**, *22*, 345–351. [CrossRef]
31. Smirnov, M.A.; Kaplan, M.A.; Sevostyanov, M.A. Receiving finely divided metal powder by inert gas atomization. *IOP Conf. Ser. Mater. Sci. Eng.* **2018**, *347*, 12033. [CrossRef]
32. Meerlender, G. Viskositäts-Temperatur-Verhalten des Standardglas I der DGG. *Glastech. Berichte* **1974**, *47*, 1–3.
33. Dinsdale, A.T.; Quested, P.N. The viscosity of aluminium and its alloys—A review of data and models. *J. Mater. Sci.* **2004**, *39*, 7221–7228. [CrossRef]
34. Gheribi, A.E.; Chartrand, P. Temperature and oxygen adsorption coupling effects upon the surface tension of liquid metals. *Sci. Rep.* **2019**, *9*, 7113. [CrossRef]

35. Lu, T.; Law, C.K. A criterion based on computational singular perturbation for the identification of quasi steady state species: A reduced mechanism for methane oxidation with NO chemistry. *Combust. Flame* **2008**, *154*, 761–774. [[CrossRef](#)]
36. Fritsching, U.; Uhlenwinkel, V. Hybrid Gas Atomization for Powder Production. In *Powder Metallurgy*; Kondoh, K., Ed.; InTech: London, UK, 2012; ISBN 978-953-51-0071-3.

Disclaimer/Publisher's Note: The statements, opinions and data contained in all publications are solely those of the individual author(s) and contributor(s) and not of MDPI and/or the editor(s). MDPI and/or the editor(s) disclaim responsibility for any injury to people or property resulting from any ideas, methods, instructions or products referred to in the content.